



Contents lists available at SciVerse ScienceDirect

## Journal of Fluids and Structures

journal homepage: [www.elsevier.com/locate/jfs](http://www.elsevier.com/locate/jfs)

## Energy harvesting from axial fluid-elastic instabilities of a cylinder

Kiran Singh\*, Sébastien Michelin, Emmanuel de Langre

Department of Mechanics, LadHyX, École Polytechnique, 91128 Palaiseau, France

## ARTICLE INFO

## Article history:

Received 19 April 2011

Accepted 26 January 2012

Available online 28 February 2012

## Keywords:

Energy harvesting

Fluid–structure interactions

Flutter instability

Reduced order models

Slender body theory

## ABSTRACT

A flexible cylindrical system unstable to flutter oscillations is analysed from the perspective of energy harvesting. In this work we analyse the non-linear reduced order model of a two-degree of freedom system of cylinders modelled with discrete stiffness and damping. The non-linear system of equations is solved in terms of cylinder deflection angles. We seek the flow speed range over which flutter oscillations are stable and correspondingly amenable to energy harvesting. Energy harvesters are modelled as viscous dashpots and the coefficients of damping are parametrised in order to determine combinations that harvest maximum power. We show that for harvesting the maximum possible energy the viscous dashpot should be placed away from the region driving the instability and for this model the optimal location is the fixed end. This result is robust to flow speed variation, action of viscous drag and to variations in cylinder geometry.

© 2012 Elsevier Ltd. All rights reserved.

## 1. Introduction

Geophysical flows in the oceans have been recently recognised as a possible energy source (Fairley, 2010), and tides in particular are appealing due to their uniformity and predictability (Westwood, 2004). Motivated by the possibility of exploiting such energy sources, in this work we analyse fluid–structure instabilities from the perspective of harvesting energy.

Recent experiments and analysis show that it is possible to generate electric power from time periodic strain deformations of a piezoelectric material actuated by flutter oscillations of an aerofoil in an external air flow. Bryant and Garcia (2011) consider a rigid aerofoil mounted on a flexible cantilevered beam with piezoelectric patches converting bending energy to electric energy. Dunnmon et al. (2011) place the piezoelectric patches on a flexible flap which is connected at the trailing edge of a rigid aerofoil. Although energy harvested from these experiments is of the order of a few milliwatts, they suggest the feasibility of energy harvesting from flutter instabilities.

The concepts discussed above consider the possibility of harvesting energy from flutter instabilities of two-dimensional plate-like structures in a flow (Païdoussis, 2004). Recently this problem has been studied in the context of flapping flags: Michelin et al. (2008) and Alben and Shelley (2008) analysed a flexible plate generating large amplitude deflections in two-dimensional inviscid flow. These studies show that flutter occurs when the destabilising action of the fluid flow overcomes the stabilising action of the internal bending stiffness of the plate. Linear stability analysis (Eloy et al., 2007) of a finite aspect ratio rectangular plate in a three-dimensional inviscid flow indicates that the flutter speed scales inversely with plate aspect ratio (ratio of span/length) and for decreasing aspect ratio it approaches the slender body limit.

\* Corresponding author. Tel.: +44 7722421001.

E-mail address: [kiran.singh@cantab.net](mailto:kiran.singh@cantab.net) (K. Singh).

In this work we are interested in flutter instabilities in slender structures immersed in a bulk flow. Experiments by [Lemaitre et al. \(2005\)](#) examined the onset of flutter in vertical ribbons of varying lengths and it was observed and confirmed theoretically that the critical flutter speed saturates to a fixed value above a certain length. This observation was also supported by the linear analysis of [de Langre et al. \(2007\)](#) for long slender flexible cylinders immersed in a flow. This work demonstrated that the inviscid fluid component in the region of high curvature is important for flutter. Viscous drag however contributes dissipation terms that act to mitigate oscillations. Experiments and non-linear analysis show that the amplitude and frequency of the limit cycle oscillations depend on system parameters such as flow speed ([Lopes et al., 2002](#); [Païdoussis et al., 2002](#); [Semler et al., 2002](#)).

The simplicity of a flexible system in an axial flowstream capable of self-sustained oscillations is attractive for energy harvesting. The main contribution of this paper is a theoretical examination of the feasibility of harvesting energy from fluttering elastic structures in axial flow using a bi-articulated link model. In this work we model energy harvesters as viscous dashpots where the damping is deformation or strain based. This is akin to the structural damping model examined by [Doaré \(2010\)](#) for pipe conveying fluids and is distinct from displacement based viscous damping (also see [Peake, 2001](#) for damping in flexible plates). Curvature based damping might be considered as a representative model for energy harvesting by strain activated materials such as piezoelectrics (see [Doaré and Michelin, 2011](#) for implementation in flexible plates).

The larger goal of this work is to analyse continuously flexible cylinders for energy harvesting. However, the theoretical and experimental work by [Benjamin \(1961a,b\)](#) on a bi-articulated pipe conveying fluid shows that canonical two degree of freedom systems can display several important characteristics of the instability observed in flexible continuous structures. In this paper we consider the bi-articulated cylindrical system immersed in a flow as a first step towards understanding energy harvesting from flexible slender structures.

In [Section 2](#) the system of equations are derived from the principle of conservation of momentum. The inviscid fluid dynamics are modelled using the theory of [Lighthill \(1971\)](#) that is valid for large amplitude deformations in slender bodies (specific care is taken to model the fluid dynamics at the articulation). The energy harvester is modelled as a viscous dashpot and the harvested energy dependence on the damping coefficients is analysed in [Section 3](#). In [Section 4](#) we include a model of the viscous drag forces exerted by the fluid on the body. We also examine the harvested power for different cylinder cross-sections and flow speeds.

## 2. Development of the fluid–structure model

Here we develop the system of equations to model the bi-articulated energy harvesting system. We consider planar motion of a pair of rigid cylinders: the first cylinder is allowed to rotate about the fixed joint  $O$  and is connected to the second cylinder through the articulation  $P$  (see [Fig. 1](#)). These articulated joints give us a two degree of freedom configuration where  $\theta_1$ ,  $\theta_2$  are the angles through which the first and second cylinders rotate about an axis perpendicular to plane ( $\mathbf{e}_x, \mathbf{e}_y$ ) at joints  $O$  and  $P$ , respectively. Energy harvesting is modelled as a viscous dashpot (damping coefficient,  $C_i$ ). Note that contrary to standard practice where a dashpot is implemented as a means to damp out oscillations, in our model it represents an energy harvester. Here we intentionally maintain distinct damping coefficients as we analyse their role on harvested power. Cylinders are modelled with equal lengths,  $L$ , torsional spring stiffness,  $K$ , and mass per unit length,  $M$ . We assume neutral buoyancy (density of the structure matches the fluid density,  $\rho$ ). The flow at infinity,  $U_\infty$ , is assumed to be uniform and directed along  $\mathbf{e}_x$ . In [Section 4](#) the fluid model is extended to include viscous drag.

In this section we develop the system of equations required to model the fluid–structure system combined with the dampers/energy harvesters. Since flutter oscillations are a non-linear phenomenon, the equations of motion are developed for large rotation angles. The rest of the paper is presented in dimensionless form, for characteristic dimensions of length,

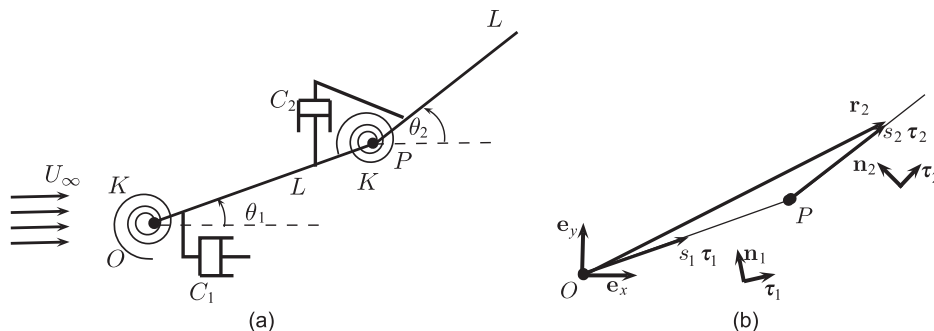


**Fig. 1.** (a) The bi-articulated cylinder model consists of a pair of cylinders of lengths,  $L$ , torsional spring stiffness,  $K$ , and viscous damping,  $C_i$ . The  $i$ th cylinder rotates through angle  $\theta_i$  relative to the fluid stream moving with velocity  $U_\infty \mathbf{e}_x$ . (b) Kinematic description used in the text: position vectors at points on the cylinders are indicated by thick solid arrows. Coordinate system  $(\mathbf{e}_x, \mathbf{e}_y)$  indicates the inertial frame of reference fixed at  $O$ ,  $(\boldsymbol{\tau}_i, \mathbf{n}_i)$  is the local tangent frame for the  $i$ th cylinder.

$L$ , mass,  $ML$ , and time,  $t^* = (ML^3/K)^{1/2}$ . Thus the non-dimensional flow speed is given as

$$u = U_\infty (ML/K)^{1/2}. \tag{1}$$

### 2.1. Formulation of governing equations

#### 2.1.1. Kinematic description

Fig. 1(b) indicates the kinematic notation adopted here. Lagrangian coordinates,  $s_i$ , uniquely identify points along the  $i$ th cylinder axis. The first cylinder is fixed at  $O$  and connected to the second cylinder at  $P$ , the second cylinder is free at the other end. The frame of reference  $(\mathbf{e}_x, \mathbf{e}_y)$  is fixed at  $O$  and defines the plane to which motion is confined.

The kinematics of a material point on the rigid cylinder is expressed in the local cylinder basis so the position vector of a point on the first cylinder is given as

$$\mathbf{r}_1(s_1, t) = s_1 \boldsymbol{\tau}_1(t), \tag{2}$$

where  $s_1$  is the Lagrangian coordinate with respect to  $O$ . Similarly we define Lagrangian coordinate  $s_2$  with respect to  $P$  with the position vector of a point on the second cylinder given as

$$\mathbf{r}_2(s_2, t) = \mathbf{r}_1(1, t) + s_2 \boldsymbol{\tau}_2(t) \tag{3}$$

and first and second partial derivatives in time are, respectively, denoted as

$$\dot{\mathbf{r}}_i = \frac{\partial \mathbf{r}_i}{\partial t} \quad \text{and} \quad \ddot{\mathbf{r}}_i = \frac{\partial^2 \mathbf{r}_i}{\partial t^2}. \tag{4}$$

#### 2.1.2. Reduced-order dynamical equations

We apply the conservation of momentum principle to derive the equations of motion for the pair of rotating rigid cylinders in contact. The expressions can be identically obtained using Hamilton's principle of least action, which is the preferred approach for similar problems (Benjamin, 1961a; Païdoussis, 1998). The principal advantage of our formulation is that we avoid the need to obtain an expression for the Lagrangian of the unbounded inviscid fluid.

Conservation of momentum applied to a system of moving rigid bodies in contact requires that the rates of change of linear momentum ( $d\mathbf{P}/dt = m\dot{\mathbf{r}}$ ) and angular momentum ( $d\mathbf{L}/dt = \partial(\mathbf{r} \wedge m\dot{\mathbf{r}})/\partial t$ ), respectively, balance the external forces and torques acting on a rigid body of mass  $m$  (Landau and Lifshitz, 1978). External forces on the  $i$ th cylinder are the fluid dynamic force,  $\int_0^l \mathbf{f}^f ds_i$ , and the contact or reaction force that manifests at the extremities. Thus applying the principle of linear momentum conservation on cylinder 2 we get

$$\int_0^1 \ddot{\mathbf{r}}_2 ds_2 = \int_0^1 \mathbf{f}_2^f ds_2 - \mathbf{F}^c, \tag{5}$$

where  $\mathbf{F}^c$  is the reaction force exerted by cylinder 1 on cylinder 2 due to contact at  $P$ . The principle of angular momentum conservation applied to cylinders 1 and 2 lead to the following equations:

$$\int_0^1 \mathbf{r}_1 \wedge \ddot{\mathbf{r}}_1 ds_1 = \int_0^1 \mathbf{r}_1 \wedge \mathbf{f}_1^f ds_1 + (\mathbf{T}_{k_1} - \mathbf{T}_{k_2}) + (\mathbf{T}_{c_1} - \mathbf{T}_{c_2}) + \mathbf{r}_1(1, t) \wedge \mathbf{F}^c, \tag{6}$$

$$\int_0^1 \mathbf{r}_2 \wedge \ddot{\mathbf{r}}_2 ds_2 = \int_0^1 \mathbf{r}_2 \wedge \mathbf{f}_2^f ds_2 + \mathbf{T}_{k_2} + \mathbf{T}_{c_2} - \mathbf{r}_1(1, t) \wedge \mathbf{F}^c. \tag{7}$$

The left hand side of (6)–(7) correspond to the inertia terms, which can be expressed in terms of the moment of inertia of the cylinders. For instance for cylinder 1:

$$\int_0^1 \mathbf{r}_1 \wedge \ddot{\mathbf{r}}_1 ds_1 = \mathcal{I} \ddot{\theta}_1 \mathbf{e}_z, \tag{8}$$

where  $\mathcal{I} = 1/3$  is the moment of inertia of cylinder 1 with respect to point  $O$ . A similar expression may be derived for cylinder 2. The stiffness and damping torques due to the  $i$ th linear spring and dashpot are given as

$$T_{k_1} = \theta_1, \quad T_{k_2} = \theta_2 - \theta_1, \tag{9}$$

and

$$T_{c_1} = c_1 \dot{\theta}_1, \quad T_{c_2} = c_2 (\dot{\theta}_2 - \dot{\theta}_1). \tag{10}$$

Using expressions (2)–(5) and substituting (9)–(10) the equations of motion (6)–(7) reduce to

$$\frac{4\ddot{\theta}_1}{3} + \frac{\ddot{\theta}_2}{2} \cos \bar{\theta} - \frac{\ddot{\theta}_2^2}{2} \sin \bar{\theta} = -2\theta_1 + \theta_2 - (c_1 + c_2)\dot{\theta}_1 + c_2\dot{\theta}_2 + \mathbf{T}_1^f, \tag{11}$$

$$\frac{\ddot{\theta}_1}{2} \cos \bar{\theta} + \frac{\ddot{\theta}_2}{3} + \frac{\dot{\theta}_1^2}{2} \sin \bar{\theta} = (\theta_1 - \theta_2) + c_2 \dot{\theta}_1 - c_2 \dot{\theta}_2 + \mathbf{T}_2^f, \quad (12)$$

where  $\bar{\theta} = \theta_2 - \theta_1$ . The fluid contribution for each cylinder is absorbed in the term  $\mathbf{T}_i^f$ , expressions for which are developed next.

## 2.2. Fluid dynamic model

The inviscid fluid dynamics are modelled using large amplitude elongated body theory (Lighthill, 1971). This theory was developed to analyse the inviscid fluid dynamics of a swimming fish, modelled by an internally actuated slender flexible cylinder generating large amplitude deformations. Recently this theory has been employed successfully in several studies that compute the pressure forces on slender bodies undergoing large amplitude deflections (Candelier et al., 2011; Eloy, in press). In particular Candelier et al. show that the model compares favourably with results from a Reynolds-averaged Navier–Stokes (RANS) numerical solver suggesting the validity of this approach for modelling large amplitude motion of slender cylinders in an inviscid flow.

The idea behind modelling the purely inviscid fluid in the first instance is to understand the fundamental aspects of energy harvesting from flutter, noting that the inviscid terms are key to triggering the flutter instability. A similar approach has been adopted in classical work on high Reynolds number (Re) fluid–structure interaction problems. For instance, Crighton and Oswell (1991) and Lucey et al. (1997) used inviscid flow models to understand fundamentals of panel flutter. In this section we briefly examine fundamental modelling aspects of the inviscid theory and then develop the fluid dynamic equations specifically applicable to the articulated rigid cylinder pair.

### 2.2.1. Lighthill's large amplitude elongated body theory

Lighthill developed the large amplitude elongated body theory to model the inviscid fluid dynamic force due to large deformations of a slender cylinder, where the measure of slenderness is the dimensionless diameter  $d \ll 1$ . The relative velocity,  $\tilde{\mathbf{u}}$ , of a point on the body is given by

$$\tilde{\mathbf{u}} = -\mathbf{u} + \dot{\mathbf{r}} = u_\tau \boldsymbol{\tau} + u_n \mathbf{n}, \quad (13)$$

where  $\mathbf{u}$  is the background velocity of the fluid. The relative velocity due to motion of a point on the body,  $\dot{\mathbf{r}}$ , is known from (2)–(4). It is convenient to express  $\tilde{\mathbf{u}}$  in tangential ( $u_\tau$ ) and normal components ( $u_n$ ).

The theory assumes that the normal component of flow velocity acts *reactively* whereas the tangential flow component acts *resistively*, where the term reactive was introduced by Lighthill to refer to the unsteady added mass contribution. Resistive terms are discussed in Section 4.1 when we model viscous drag. An expression for the reactive force distribution,  $\mathbf{f}^f$ , exerted by the fluid in contact with the cylindrical element can be defined in terms of the normal reactive momentum,  $m_a u_n$ . Note that  $m_a = M_a/M$ , where  $M_a$  is the dimensional added mass per unit length, the added mass being defined as the fluid mass accelerated along with the moving cylinder (Lighthill, 1960). Unless otherwise specified we assume cylinders of circular cross-section ( $m_a = 1$ ). A key assumption of this theory is that if the radius of curvature is much larger than the cross-wise dimension then the force exerted by the fluid on a point on the body at  $\mathbf{r}$  only depends upon  $\tilde{\mathbf{u}}(\mathbf{r})$  and the cross-sectional dimensions local to  $\mathbf{r}$ .

Lighthill states that the total reactive fluid force acting on the body may be determined by the application of the principle of momentum conservation on the volume of fluid surrounding the body ahead of the trailing edge—thereby ignoring wake induced effects. More generally, momentum conservation on an arbitrary cross-section gives us an expression for reactive force,  $\mathbf{f}^f$ , acting at that section. By the principle of momentum conservation the contributions of the following components must sum to zero: (i) the rate of change of momentum within the fluid volume,  $dV$ , (ii) the normal momentum flux convected out of  $dV$ , (iii) the pressure force acting on the surface bounding  $dV$  and (iv) the reactive force,  $\mathbf{f}^f$ , exerted by the fluid on the structure. Thus we get

$$\mathbf{f}^f(s, t) = -\left( \frac{\partial m_a u_n \mathbf{n}}{\partial t} + \frac{\partial m_a u_n (-u_\tau) \mathbf{n}}{\partial s} + \frac{1}{2} \frac{\partial m_a u_n^2 \boldsymbol{\tau}}{\partial s} \right). \quad (14)$$

Contributions (i), (ii), (iii) correspond to the first, second and third terms, respectively, on the right hand side in (14). Here  $\mathbf{f}^f$  includes non-linear terms due to large amplitude motion of the structure. Cylinders are allowed to rotate through large angles, however we impose the condition  $|\theta_i| < \pi/2$ , such that the tangential component of the flow velocity is positive. This condition is employed to ensure the validity of the fluid model, noting that the premise of Lighthill's theory is that lateral motion occurs in a flowstream where the tangential component is advected downstream from the body.

### 2.2.2. Fluid dynamic equations for the bi-articulated system

We split the inviscid fluid dynamic force into contributions due to the relative flow over (a) the rigid cylinders and (b) the transition region over the articulation at  $P$ . Expressions for fluid force over the rigid cylinders 1 and 2 are, respectively,

$$\mathbf{F}_1^f = \int_0^1 \mathbf{f}_1^f ds_1 = -m_a \left( \frac{1}{2} \ddot{\theta}_1 + 2u \dot{\theta}_1 \cos \theta_1 \right) \mathbf{n}_1,$$

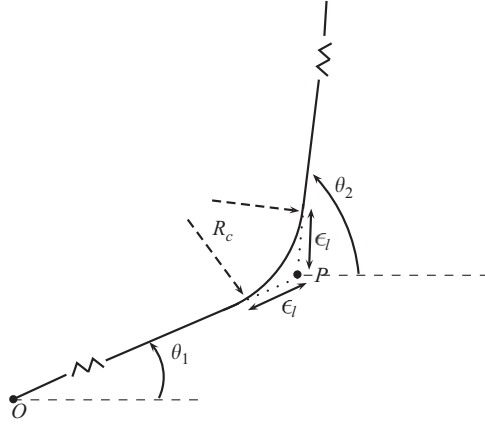


**Fig. 2.** A close-up view of the transition over the articulation region of length  $\epsilon_l \ll 1$  for modelling the fluid dynamics. Radius of curvature in this region is defined as  $R_c > \epsilon_l$ , dotted lines indicate the rigid cylinder geometry near  $P$  corresponding to the structural model indicated in Fig. 1(a).

$$\mathbf{F}_2^f = \int_0^1 \mathbf{f}_2^f ds_2 = -m_a \left( \ddot{\theta}_1 \cos \bar{\theta} + \dot{\theta}_1^2 \sin \bar{\theta} + \frac{1}{2} \ddot{\theta}_2 - 2\dot{\theta}_1 \dot{\theta}_2 \sin \bar{\theta} + 2u \dot{\theta}_2 \cos \theta_2 \right) \mathbf{n}_2. \quad (15)$$

The fluid contribution in the curvature region requires closer scrutiny. We develop an expression for this component by assuming that the transition in angle from  $\theta_1$  to  $\theta_2$  at joint  $P$  occurs over a length  $2\epsilon_l$  along which the curvature varies smoothly (where  $\epsilon_l \ll 1$ , see sketch Fig. 2). The conditions,  $d \ll \epsilon_l \ll 1$ , and,  $R_c \geq \epsilon_l$ , for  $\bar{\theta} < \pi/2$  satisfy the assumptions of Lighthill's theory. Integrating  $\mathbf{f}^f$  over this region gives a point force at  $P$  at leading order. The torque exerted by this term will be  $\mathbf{r}_1(1,t) \wedge \mathbf{F}_J + O(\epsilon_l)$ , where

$$\begin{aligned} \mathbf{F}_J &= -m_a \int_{1-\epsilon_l}^{1+\epsilon_l} \left( \frac{\partial u_n \mathbf{n}}{\partial t} - \frac{\partial u_n u_\tau \mathbf{n}}{\partial s} + \frac{1}{2} \frac{\partial u_n^2 \boldsymbol{\tau}}{\partial s} \right) ds, \\ &= \frac{1}{2} (u \sin \theta_1)^2 \boldsymbol{\tau}_1 - \frac{1}{2} (\dot{\theta}_1 \cos \bar{\theta} + u \sin \theta_2)^2 \boldsymbol{\tau}_2 + (\dot{\theta}_1 u \cos \theta_1 + u^2 \sin \theta_1 \cos \theta_1) \mathbf{n}_1 \\ &\quad + (\cos \bar{\theta} \sin \bar{\theta} (\dot{\theta}_1^2 - u^2) - u \cos(2\theta_2 - \theta_1) \dot{\theta}_1) \mathbf{n}_2 + O(\epsilon_l). \end{aligned} \quad (16)$$

For compactness we include contributions from  $\mathbf{F}_J$  into the equations for cylinder 1. Combining (15) and (16), expressions for the fluid dynamic terms in (11) and (12) are, respectively,

$$\begin{aligned} \mathbf{T}_1^f &= \int_0^1 \mathbf{r}_1 \wedge \mathbf{f}_1^f ds_1 + \mathbf{r}_1(1,t) \wedge \int_0^1 \mathbf{f}_2^f ds_2 + \mathbf{r}_1(1,t) \wedge \mathbf{F}_J \\ &= -m_a \left( \frac{\sin 2\bar{\theta}}{2} \dot{\theta}_1^2 + \left( \frac{1}{3} + \cos^2 \bar{\theta} \right) \ddot{\theta}_1 + \frac{\ddot{\theta}_2}{2} \cos \bar{\theta} + u \dot{\theta}_1 \cos \theta_1 + 2u \dot{\theta}_2 \cos \theta_2 \cos \bar{\theta} - \dot{\theta}_1 \dot{\theta}_2 \sin 2\bar{\theta} \right) \mathbf{e}_z + \mathbf{r}_1(1,t) \wedge \mathbf{F}_J, \end{aligned} \quad (17)$$

$$\mathbf{T}_2^f = \int_0^1 s_2 \boldsymbol{\tau}_2 \wedge \mathbf{f}_2^f ds_2 = -m_a \left( \frac{\sin \bar{\theta}}{2} \dot{\theta}_1^2 + \frac{\cos \bar{\theta}}{2} \ddot{\theta}_1 + \frac{\ddot{\theta}_2}{3} + u \dot{\theta}_2 \cos \theta_2 - \dot{\theta}_1 \dot{\theta}_2 \sin \bar{\theta} \right) \mathbf{e}_z. \quad (18)$$

Retaining  $O(1)$  terms in  $\mathbf{F}_J$  we get

$$\mathbf{r}_1 \wedge \mathbf{F}_J = m_a \left( \frac{1}{4} \dot{\theta}_1^2 \sin 2\bar{\theta} \cos \bar{\theta} + u (\cos \theta_1 - \cos^2 \bar{\theta} \cos \theta_2) \dot{\theta}_1 + \left( \sin 2\theta_1 - \sin \theta_2 \cos \theta_1 - \frac{1}{2} \sin 2\theta_2 \cos \bar{\theta} \right) \frac{u^2}{2} \right) \mathbf{e}_z. \quad (19)$$

Substituting fluid dynamic expressions, (17)–(18), into equations of motion, (11)–(12), we solve for the system response,  $\theta_1$  and  $\theta_2$ .

### 2.3. Solution of the equations of motion for zero damping

Eqs. (11)–(12) are second-order non-linear ordinary differential equations in time with variables  $\theta_1, \theta_2$ . We solve these numerically using a Runge–Kutta ode45 solver in MATLAB with a relative error tolerance of  $10^{-6}$ . The calculations are initiated with a perturbation from the rest state, and the integration is stopped if either  $\bar{\theta} < \pi/2$  or  $|\theta_i| < \pi/2$  is violated.

To test the implementation we first consider the case of no structural damping ( $c_i=0$ ) and examine the basic fluid–structure response. Fig. 3(a) shows the system response to increasing flow speed,  $u$ . We calculate a critical flow speed of  $u^{cr} \approx 2.13$ , below which the fluid acts to damp out disturbances imparted to the system. At  $u^{cr}$  the system undergoes a

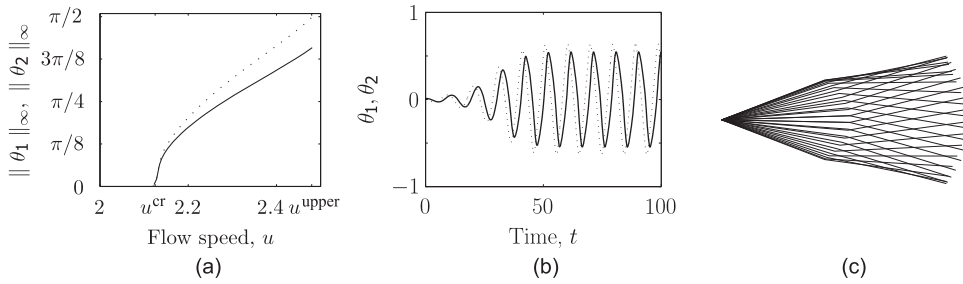


**Fig. 3.** In (a) the variation of  $\|\theta_i\|_\infty$  ( $i = 1, 2$ ) with  $u$  shows the onset of flutter above  $u^{cr} = 2.13$  ( $u^{upper} = 2.48$ ). In plots (a) and (b) solid curves correspond to  $\theta_2$ , dotted curves to  $\theta_1$ . Shown in (b) and (c) is the flutter response of the system at  $u = 2.2$ : the time series response to an initial perturbation is plotted in (b); in (c) the bi-articulated system in flutter is indicated by superimposed snapshots of the system at successive time intervals during an oscillation period.

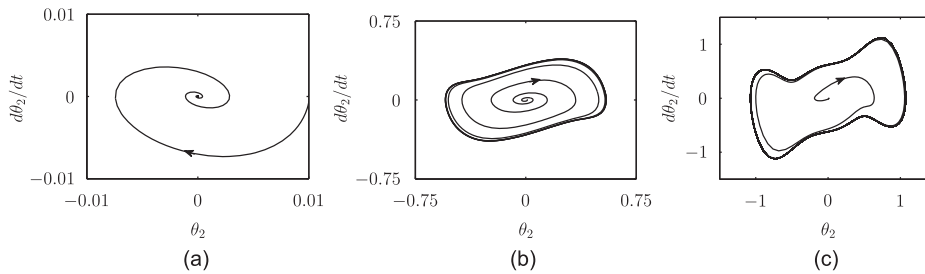


**Fig. 4.** Phase-plane plots show the change in topological structure with increasing flow speed. In (a)  $u = 2.0$  and is below  $u^{cr}$  whereas limit cycles emerge above  $u^{cr}$  as seen for (b)  $u = 2.2$  and (c)  $u = 2.4$ .

Hopf bifurcation and at higher velocities we see steady flutter oscillations as in Fig. 3(b). A physical picture of these oscillations can be seen from Fig. 3(c) where we superimpose snapshots in time of the bi-articulated cylindrical position. Note that the linear equations for the bi-articulated pipe conveying fluid system and the bi-articulated cylinders in a flow are identical for an inviscid fluid, and so the critical flutter speeds must agree. This result is consistent with the prediction of Benjamin (1961a), once the differing non-dimensionalisations are accounted for with the multiplication factor of  $\sqrt{3/(1+m_a)}$ . The upper limit,  $u^{upper} \approx 2.48$ , corresponds to the flow speed at which  $\theta_1 = \pi/2$  and calculations terminate above this flow speed in accordance with the criterion discussed in Section 2.2.1.

Linear analysis shows that if  $\mathbf{F}_j$ , the inviscid component of the force at articulation point  $P$  is neglected, flutter oscillations are not predicted at any flow speed (de Langre et al., 2007). Fig. 3(b) shows that the oscillation cycle of the second cylinder lags in phase behind the first cylinder (Fig. 3(c) helps visualise this motion). Thus this might be interpreted as positive work being done on the structure by  $\mathbf{F}_j$ , the inviscid fluid force contribution from the articulation at  $P$ .

Phase plots in Fig. 4 indicate the change in topological structure of the dynamical system with  $u$ . Below  $u^{cr}$  (Fig. 4(a),  $u = 2$ ) the equilibrium point is a stable focus, at  $u^{cr}$  it switches stability to an unstable focus and above this speed a stable limit cycle emerges (Fig. 4(b),  $u = 2.2$ ). The limit cycle becomes increasingly tortuous at higher speeds (Fig. 4(c),  $u = 2.4$ ) and the solution is terminated for values of  $u > u^{upper}$  as angles exceed  $\pi/2$ , the condition that renders Lighthill's model as invalid.

These results show a simple picture of the onset and evolution of the flutter instability with varying flow speeds. In Section 3 we analyse the power response at a fixed value of flow speed ( $u = 2.45$ ).

### 3. Results: Harvesting energy from an inviscid fluid

We next investigate harvesting of energy from the flutter instabilities observed above critical speeds in the bi-articulated cylindrical system. Energy harvesters are modelled as viscous dashpots as noted in Section 2, henceforth these expressions are used interchangeably.

The energy dissipated in a viscous damper gives an expression for the time-averaged power harvested over a period of oscillation,  $T$  (Landau and Lifshitz, 1978):

$$\mathcal{P} = \frac{1}{T} \int_0^T [c_1 \dot{\theta}_1^2 + c_2 (\dot{\theta}_1 - \dot{\theta}_2)^2] dt. \quad (20)$$

$\mathcal{P}$  is the sum of individual contributions from the two harvesters,  $\mathcal{P}_1$  and  $\mathcal{P}_2$ , corresponding to the first and second terms in expression (20), respectively. We evaluate these contributions for varying values of  $c_1$  and  $c_2$  in order to understand the harvested power dependence on damping.

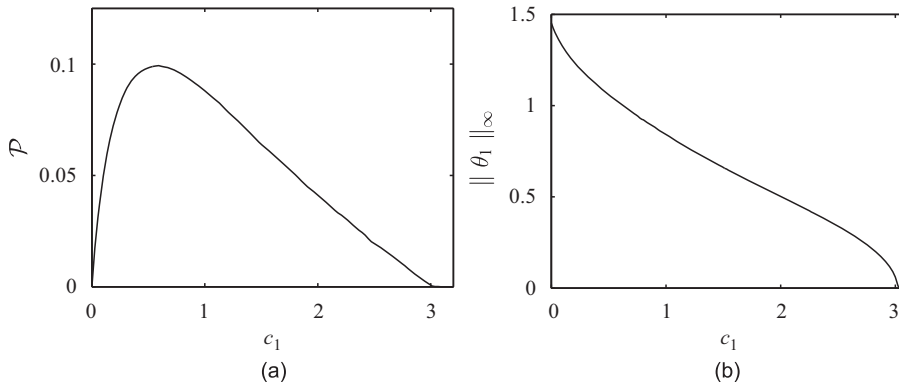


**Fig. 5.** (a) Harvested power,  $\mathcal{P}$  and (b)  $\|\theta_1\|_\infty$  variation with damping coefficient  $c_1$  for a single harvester case ( $c_2 = 0$ ). Computations are performed at flow speed,  $u=2.45$ .

### 3.1. Power response for one harvester

First we introduce one damper at the fixed end  $O$ . Thus  $c_2 = 0$  and  $c_1$  is varied from zero to a value above which oscillations are completely damped out. The power harvested and system response to increasing  $c_1$  are indicated in Fig. 5. The power curve in Fig. 5(a) shows an intermediate peak, which establishes the existence of an optimum damping coefficient ( $c_1^{\text{opt}} \approx 0.6$ ) at which harvested power is maximum. The intermediate peak in power is consistent with the expression in (20) and the system response–power is neither harvested for  $c_1 = 0$  since none of the mechanical energy of oscillations is transferred to the dashpot nor for  $c_1 \geq 3.05$  as oscillations are completely mitigated owing to excessive damping. Fig. 5(b) illustrates that the process of energy harvesting in this system causes a reduction in the amplitude of oscillations. It is worth noting that for each flow speed there is a unique  $c_1^{\text{max}}$  and  $c_1^{\text{opt}}$ , and these are increasing functions in  $u$ .

### 3.2. Power response for two harvesters

We next introduce a second harvester at movable joint  $P$  in order to investigate the possibility of generating additional power over the maximum value predicted for a single harvester. Thus  $\mathcal{P}$  is computed for all combinations of  $c_1$  and  $c_2$  and from Fig. 6(a) we see that the peak power value lies on the  $c_1$ -axis. We may conclude that for any  $c_2 \neq 0$  the maximum possible power that may be harvested is lower than the corresponding maximum power for a single-damper system. Superimposed on the power map is the stability boundary predicted by linear theory that shows the combinations of  $c_1$  and  $c_2$  above which flutter oscillations are completely damped out, so no power is harvested. As for the case of a single harvester, the upper bounds on the damping coefficients for the two harvesters also increase with flow speed.

We examine the contribution from both joints by plotting the power variation with  $c_2$  at  $c_1^{\text{opt}}$ . In Fig. 6(b) the total power,  $\mathcal{P}$ , and individual contributions,  $\mathcal{P}_1$  and  $\mathcal{P}_2$ , are plotted. It should be noted that the dominant contribution to  $\mathcal{P}$  comes from  $\mathcal{P}_1$ . Although  $\mathcal{P}_2$  displays a maximum at an intermediate value of  $c_2$ , it is insufficient to counter the sharp reduction in  $\mathcal{P}_1$  associated with the net decrease of flapping amplitude induced by the introduction of  $c_2$ . Hence the total power decreases monotonically with  $c_2$ .

The power and oscillation amplitude variation with  $c_1$  as plotted in Fig. 5 is representative of the competitive elements involved in energy harvesting in the idealised fluid. From the expression for the harvested power (20) we see that adding more structural damping increases the proportion of the energy harvested, but the process of harvesting energy necessarily mitigates the oscillatory response. The challenge lies in identifying an optimal balance between these competing effects.

### 3.3. Linear stability analysis of differential dashpot contribution

The surprising outcome of the above computations is that for the bi-articulated system with identical cylinder length and spring stiffness there lies a preferred position for placement of energy harvesters. To probe this observation further we look to the linearised system for a possible explanation. One notes that the linear flutter response differs significantly from the non-linear configuration as only the onset of the Hopf bifurcation can be predicted in the linear case and not the limit cycle itself. Nonetheless, the linear solution can give clues as to reasons for the differing response of the system. In Fig. 7(a) we plot the growth rate,  $\sigma$ , of the most unstable mode as a function of  $c_1$  and  $c_2$ . The variation of the growth rate with damping reflects the differing contributions of each dashpot on the total harvested power, and  $c_2$  emerges as the dominant oscillation mitigating parameter. The curves in Fig. 7(b) indicate the variation of  $\sigma$  along the abscissa and ordinate of the map and clearly portray the different actions of the two dashpots as the neutral curve is approached. We see a sharp

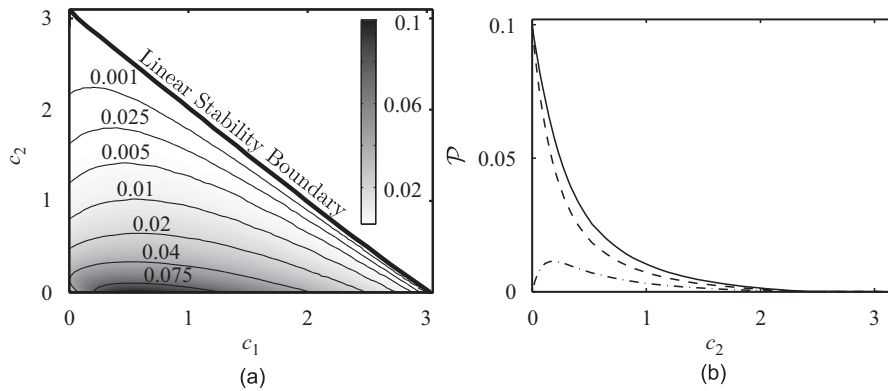


**Fig. 6.** At flow speed,  $u=2.45$ , the (a) power contours for the useful range of  $c_1$  and  $c_2$  are shown. The linear stability curve indicates limiting combinations of  $c_1$  and  $c_2$  above which oscillations do not occur. In (b) the plot of the variation in harvested power with  $c_2$  (at  $c_1^{\text{opt}} = 0.6$ ) is indicated. The solid curve represents the total power,  $P$ , dashed curve corresponds to  $P_1$ , dashed-dot curve to  $P_2$ .

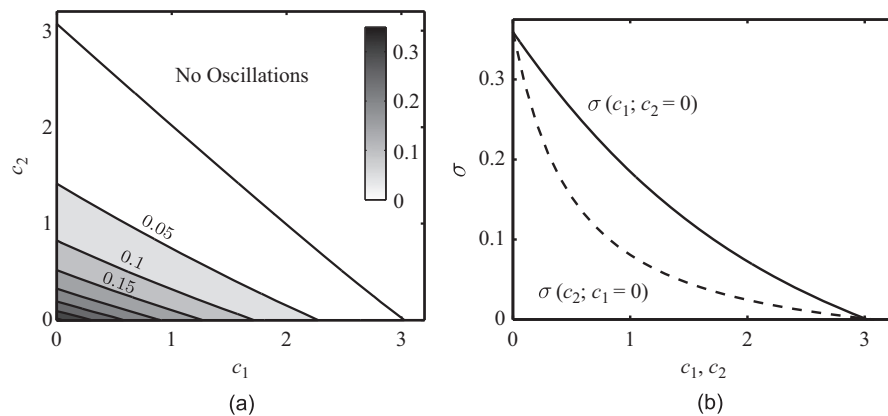


**Fig. 7.** Growth rate  $\sigma$  of the most unstable mode computed from the linear dispersion relation for the configuration in Fig. 6. In (a)  $\sigma$  is mapped for all combinations of  $c_1, c_2$  (with a uniform contour line spacing of 0.05); in (b) we show curves of  $\sigma$  for variation in  $c_1$  ( $c_2 = 0$ , solid curves) and  $c_2$  ( $c_1 = 0$ , dashed curves).

reduction in growth rate for small  $c_2$  in contrast to the more gradual reduction with  $c_1$ ; an indication of the effective damping properties of a dashpot at  $P$ . From the perspective of energy harvesting this result leads us to conclude that a dashpot at joint  $P$  is less effective in harvesting energy than a dashpot at  $O$ .

From a physical perspective the differing influence of  $c_1$  and  $c_2$  appears to originate from the source of the instability. As noted in Section 2.3, the inviscid fluid near the articulation region  $P$  works to destabilise the system to flutter. A viscous dashpot placed near the source of the instability has a strong damping effect. Thus the condition to maximise energy harvesting from the bi-articulated system requires the placement of a viscous dashpot away from the region driving the instability and for this reduced order model we find the optimal point to be the fixed articulation  $O$ . This model also shows that the optimal damping coefficient depends on flow speed. In the next section we confirm these results with a more representative fluid model that includes the viscous fluid dissipation term.

#### 4. Drag modelling and parameter variation

As discussed in Section 2, the large amplitude elongated body theory assumes that the normal flow component contributes to the inviscid force whilst the tangential component contributes to resistive drag. In Section 4.1 we apply the resistive force theory of Taylor (1952) to analyse the role of drag on changing the flutter response and harvested power. We then extend the parameter space to understand the impact of variation in cross-sectional geometry of the cylinders in Section 4.2. In Section 4.3 we compute the peak power harvested at different flow speeds.

##### 4.1. Drag model

Integration of the viscous stresses acting on a solid body moving relative to the fluid manifests as a drag force. We calculate this drag using the resistive force theory of Taylor (1952) which posits that there are two main contributions to

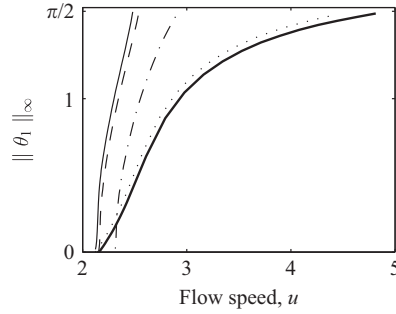


**Fig. 8.** Effect of drag on the transition to flutter: The bifurcation curves show the  $\|\theta_1\|_\infty$  variation with increasing flow speed,  $u$ , for the inviscid case (thin solid curve),  $C_f = 0.01$ ,  $C_{D,p} = 0$  (dashed curve)  $C_f = 0.05$ ,  $C_{D,p} = 0$  (dashed-dot curve),  $C_f = 0$ ,  $C_{D,p} = 1.0$  (dotted curve),  $C_f = 0.01$ ,  $C_{D,p} = 1$  (thick solid curve).

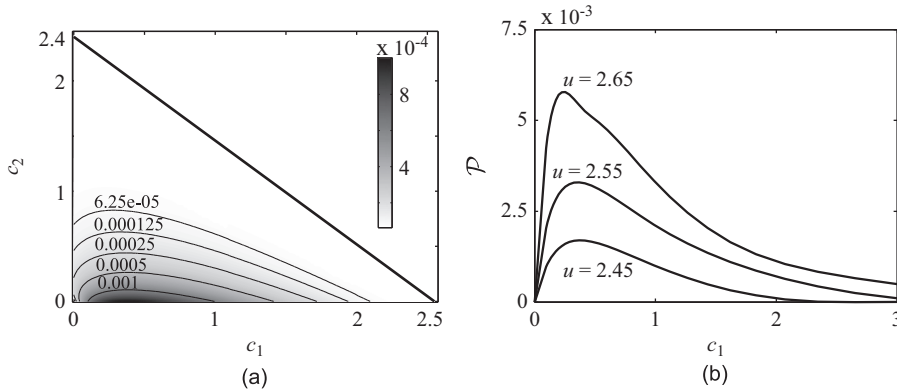


**Fig. 9.** Effect of drag on energy harvesting: (a) Variation of  $\mathcal{P}$  for varying  $c_1$  and  $c_2$  at  $u = 2.45$ , (b)  $\mathcal{P}$  variation with  $c_1$  ( $c_2 = 0$ ) for different values of  $u$  (for all cases the drag coefficients  $C_f = 0.01$ ,  $C_{D,p} = 1.0$ ).

drag: (i) *friction* drag due to tangential viscous stresses exerted by the fluid on the body, and (ii) *form* or *parasitic* drag due to the normal stress exerted on the body due to its motion relative to the fluid (also see Sherman, 1990). Taylor’s calculations suggest that the rough cylinder model is appropriate for  $Re > 10^5$  thus here we assume a rough cylinder. We use Taylor’s scaling for dimensional parasitic drag per unit length,  $\rho D U_n |U_n|$ , where  $D$  is the cross-sectional diameter noting that Taylor’s model for parasitic drag is unambiguously adopted in the literature. However, the friction drag term appears to be open to interpretation, in all likelihood due to Taylor’s speculation as to the choice of the empirical roughness parameter. In order to implement a model of friction drag for large amplitude motion we turn to the model of Kambe (1978) for the tangential friction drag. Here we extend it to include the normal component, and we note that the dimensional friction drag per unit length scales as  $\rho D U_\tau \mathbf{U}$ . Combining these two components, the non-dimensional expressions for tangential and normal drag for the  $i$ th cylinder are, respectively,

$$\mathbf{D}_i^f = \frac{m_a}{2\pi d} C_f u_{\tau,i}^2 \boldsymbol{\tau}_i, \quad \mathbf{D}_i^n = \frac{m_a}{2\pi d} (C_f u_{n,i} u_{\tau,i} - C_{D,p} u_{n,i} |u_{n,i}|) \mathbf{n}_i, \tag{21}$$

where, consistently with the slender cylinder assumption, we define the slenderness parameter,  $d = 0.1$ . Here  $C_f$  is the friction drag coefficient and  $C_{D,p}$  is the parasitic drag coefficient. Equations of motion (11)–(12) are modified to include drag. For brevity these expressions are not re-derived here. It is worth noting that Boyer et al. (2008) use a similar approach as adopted here and agreement with their RANS computations suggests that the combined reactive-resistive theory is a valid model for slender structures in the high  $Re$  regime.

In the literature, the parasitic drag coefficient is typically  $\sim O(1)$  and the rough cylinder ( $Re > 10^5$ ) friction drag coefficient is  $\sim O(10^{-2})$  (Boyer et al., 2008; de Langre et al., 2007; Taylor, 1952). As observed from the inviscid fluid analysis, the bifurcation curve for the unharvested system gives a general idea about the range of  $u$  in which flutter oscillations occur, and the amplitude of oscillation at specific values of  $u$ . In Fig. 8 we plot this curve for representative values of  $C_f$  and  $C_{D,p}$  (for  $c_i = 0$ ). Friction drag is seen to be stabilising as the oscillatory instability sets in at higher values of flow speed as compared to the zero drag case. Parasitic drag does not change the critical flow speed, but at a particular  $u$  it reduces the amplitude of oscillations. We observe that drag acts to extend the range of operating flow speed for which the oscillation amplitudes lie within accepted bounds. As in Section 2.2.1, the criterion for the assumptions of this model to

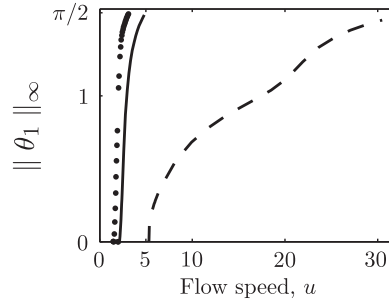


**Fig. 10.**  $\|\theta_1\|_\infty$  variation with flow speed for:  $m_a=1.0$  (solid curve),  $m_a=2.0$ , (dotted curve) and  $m_a=0.1$  (dashed curve). Here  $c_1=c_2=0$  and drag coefficients,  $C_f=0.01$ ,  $C_{D,p}=1.0$ .

remain valid is  $\|\theta_1\|_\infty < \pi/2$ . Based on the results in Fig. 8, we select  $C_f=0.01, C_{D,p}=1$  for the drag model in the remainder of this work.

In Fig. 9(a) we plot the power harvested for varying combinations of  $c_1$  and  $c_2$ . Comparisons with the purely inviscid case (Fig. 6) at the same flow speed ( $u=2.45$ ) show that the qualitative dependence of harvested power on  $c_1$  and  $c_2$  does not change. As observed for the inviscid computations, the optimal value at which maximum power is harvested also lies on the  $c_1$  axis ( $c_2=0$ ). However, quantitative differences are significant: at the same flow speed we see a reduction in power by almost two orders of magnitude when drag is included. Despite this reduction at a fixed  $u$ , Fig. 8 shows that the flow speed range in which flutter oscillations are observed is significantly larger. As a consequence, energy harvesting is possible at speeds that exceed the limits for a purely inviscid fluid. Thus, with the inclusion of drag higher values of non-dimensional power are achieved in a higher  $u$  range. This can be seen from Fig. 9(b) where we plot the power response as a function of  $c_1$  for various values of  $u$ . This result effectively captures the contradictory roles of viscous drag: its dissipative action effects a reduction in the power available for harvesting energy whilst its stabilising action leads to sustained flutter oscillations of suitable amplitudes over a wider range of flow speeds, far exceeding the range of  $u$  for the inviscid fluid. Thus we find that the stabilising action allows for higher values of power to be harvested. In Section 4.3 we examine this dependence of  $\mathcal{P}$  on  $u$ .

#### 4.2. Variation in mass ratio

For neutrally buoyant cylinders of non-circular cross-sections the mass ratio differs from 1. For instance, an elliptical cross-section with  $m_a > 1$  will have the major axis of the ellipse directed perpendicular to the plane of motion (conversely parallel for  $m_a < 1$ ). In this section we repeat the computations in Section 4.1 for two elliptical cross-sections. A change in cross-section geometry warrants a representative change in values of the empirical drag coefficients; a possible approach in choosing these values was demonstrated by Boyer et al. (2008). However, this study also showed that the order of magnitude of the coefficients does not vary greatly with change in geometry. Bearing in mind the exploratory nature of our work and in the interest of consistency in this study we use the circular cylinder drag coefficients.

The non-linear response for selected values of mass ratio may be understood from the bifurcation curve in Fig. 10. Compared to  $m_a=1$ , the critical flutter speed decreases for  $m_a=2$ , we see a shrinking of the flow speed range over which flutter oscillations are observed and oscillation amplitudes grow rapidly above  $u^c$ . Conversely, for  $m_a \leq 1$  oscillation amplitudes grow more gradually, the useful flow speed range increases and flutter onset is delayed to higher flow speeds. The discontinuity in the curve at  $m_a=2$  corresponds to a small  $u$  range over which the bi-articulated system transitions from limit cycle oscillations to divergence. Outside this range, divergence disappears and flutter oscillations are observed (this is not a unique observation, see Semler et al., 2002). We proceed by selecting the appropriate values of  $u$  to analyse power dependence on  $c_1$  and  $c_2$ .

In Fig. 11 we plot the power response for  $m_a=2$  at  $u=2.42$ . Compared to the nominal case ( $m_a=1$ , Fig. 9) we see that peak power is harvested at a lower value of  $c_1$ . Close to the stable boundary there is an abrupt reduction in power for a marginal increase in  $c_1$ , which is seen in Fig. 11(b). Dynamically, the discontinuity arises due to a switch in the equilibrium state as symmetric flutter transitions to an asymmetric flutter mode.

Computations reveal that this onset of asymmetric flutter is observed in the higher range of  $u$ . Whereas the onset of asymmetric flutter is associated with a reduction in harvested power for  $m_a=2$ , it results in an increase in power for  $m_a \leq 1$ . We see this increase in power for  $m_a=0.1$  in Fig. 11(c) and (d) where the map reflects the two regimes of symmetric and asymmetric flutter segregated by a cusp in the power contours. Switching occurs at a comparatively small value of damping as compared to the final damping coefficient above which all oscillations are mitigated. And although for  $c_2=0$  the discontinuity manifests at  $c_1 \sim 1$ , we find that asymmetric flutter is the only stable mode for high enough values of structural damping, as is evident from the curve at  $c_2 \sim 0.9$ . It must be emphasised that asymmetric flutter is not restricted to  $m_a$  values that differ from unity. Although we do not see the jump in the power curves in Fig. 9(b), the phenomenon appears in the high flow speed range ( $u > 2.7$  for  $m_a=1$ ).

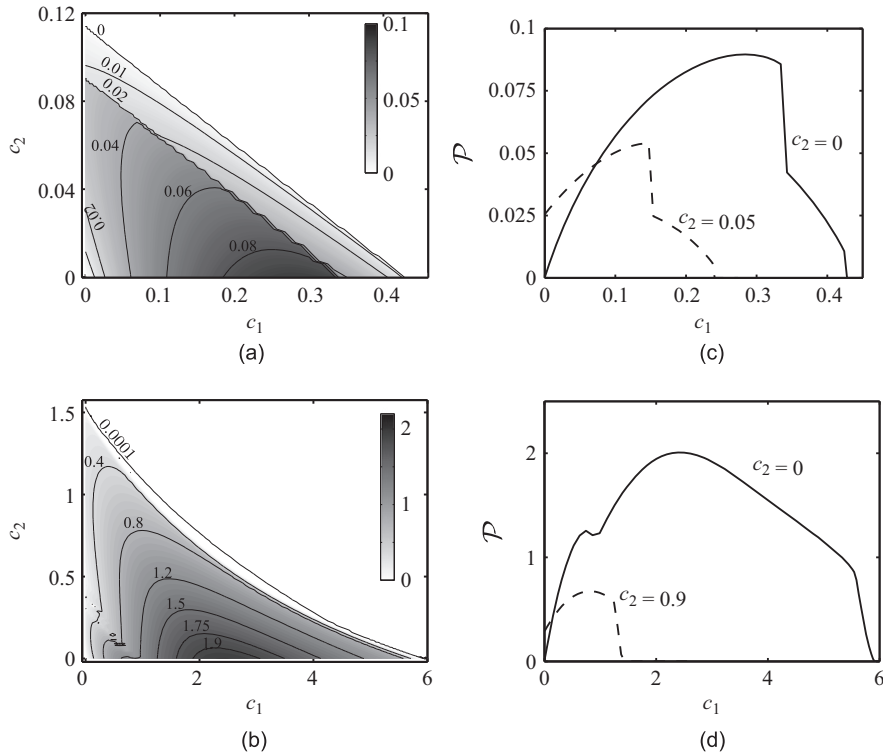


**Fig. 11.** Harvested power dependence on mass ratio: Power contour maps and curves are indicated for  $m_a=2.0$  at flow speed  $u=2.42$  in (a) and (b) and  $m_a=0.1$  at flow speed  $u=11.1$  in (c) and (d), respectively (drag coefficients  $C_f=0.01$ ,  $C_{D,p}=1.0$ ).

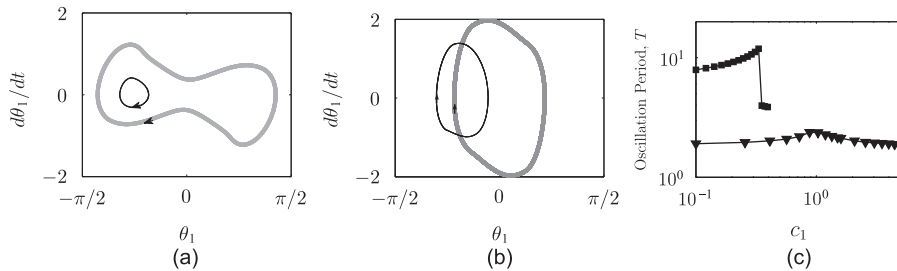


**Fig. 12.** System response for symmetric (thick grey lines) and asymmetric flutter (black lines) is captured in the  $\theta_1$  phase-plane plots for: (a)  $m_a=2.0$  at  $u=2.42$  with damping coefficients  $c_1=0.2$  (grey) and  $c_1=0.4$  (black) and (b)  $m_a=0.1$  at  $u=11.1$  and  $c_1=0.4$  (grey) and  $c_1=2.5$  (black). In (c) the variation of oscillation period with  $c_1$  for  $m_a=2.0$  (squares) and  $m_a=0.1$  (inverted triangles) is indicated. Note: For all figures  $c_2=0$ .

In Fig. 12(a) and (b) we compare the phase–plane plots for both cross-sections prior to and after the onset of asymmetric flutter. For both  $m_a$  the limit-cycle plotted for asymmetric flutter is one of a pair and which of the pair is triggered depends on the sign of the initial perturbation (we have checked to ensure that the time averaged power is the same for both). The phase–plane plots suggest that the transition from asymmetric to symmetric flutter occurs through different global bifurcations, this is observed from the oscillation period variation as well in Fig. 12(c) where the discontinuities in the curves indicate the bifurcation points. It is interesting to note that asymmetric flutter corresponds to a reduction in oscillation period with increasing  $c_1$  for both  $m_a$ .

The power map in Fig. 11(c) also indicates islands of zero power, which correspond to non-deterministic behaviour (no relevant time scale of oscillation can be determined). These occur in the regime of small structural damping and are due to the transition from symmetric to asymmetric flutter via a chaotic route. Despite these obvious differences observations suggest that the essential characteristics of power harvested from flutter are very similar to the purely inviscid case analysed in Section 3. Peak values of power are generated for intermediate values of  $c_1$  at zero  $c_2$  and the value of the optimal damping coefficient,  $c_1^{opt}$ , corresponding to peak power varies with  $u$ . We also note here that the reduction in critical flow speed with  $m_a$  is apparently at odds with the results of Paidoussis (1998, see Section 3.8.2). The apparent anomaly arises due to differences in non-dimensionalising parameters used in the two analyses. This leads to expressions for non-dimensional flow speeds that differ by a multiplication factor of  $m_a^{1/2}$ .

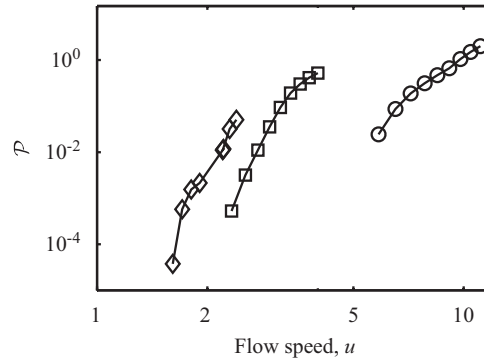


**Fig. 13.** Non-dimensional peak power variation with flow speed at three different values of mass ratio:  $m_a = 0.1, 1, 2$  represented by circle, square and diamond symbols, respectively (drag coefficients:  $C_f = 0.01$ ,  $C_{D,p} = 1.0$ ).

**Table 1**

Dimensional power for different cylinder lengths of mass  $M = \rho\pi D_1 D_2 / 4$ . Two cross-sections are compared: Column (I): circular cross-section,  $D_1 = D_2 = L/10$ , Column (II): elliptical cross-section  $D_1 = L/\sqrt{10}$ ,  $D_2 = D_1/10$ . Other dimensional quantities are  $U_\infty = 1$  m/s,  $K = 1$  N-m,  $\rho = 10^3$  kg/m<sup>3</sup>.

$L$ (m)	$P_{\text{harv}}$ (W)	
	(I)	(II)
1.0	$4 \times 10^{-3}$	$7.5 \times 10^{-2}$
1.1	$3 \times 10^{-2}$	$1.2 \times 10^{-1}$
1.2	$8 \times 10^{-2}$	$1.8 \times 10^{-1}$
1.3	$2 \times 10^{-1}$	$2.5 \times 10^{-1}$

#### 4.3. Dependence on flow speed

The bifurcation curves in Fig. 10 reveal that for a given geometric configuration there is a range of flow speeds over which energy can be harvested. To investigate how power harvested varies with  $u$ , in Fig. 13 we calculate peak power harvested in the flow speed range for which flutter oscillations are observed. We compute power for three values of mass ratio,  $m_a = 0.1, 1, 2$ . We find that a reduction in mass ratio leads to a wider range of flow speeds over which flutter is observed as well as an increase in peak power, particularly useful from an energy harvesting standpoint. Recall that the upper limit on flow speed comes from the constraint  $\|\theta_i\|_\infty < \pi/2$ .

An expression for the dimensional harvested power,  $P_{\text{harv}}$ , can be obtained from dimensional analysis:

$$P_{\text{harv}} = \frac{K^{3/2}}{L^{3/2} M^{1/2}} \mathcal{P}(U_\infty (ML/K)^{1/2}, M). \quad (22)$$

We compute dimensional values of power for varying cylinder lengths and two cross-sections,  $m_a = 1, 0.1$ , with values of flow speed,  $U_\infty$ , and torsional spring stiffness,  $K$ , as indicated in Table 1. It is worth noting here that the value of  $U_\infty$  is constrained by typical tidal or river currents speeds, hence the geometric dimensions of the cylinder emerge as useful parameters.

The tabulated values show the sensitivity of the power to variations in length. Expression (22) may suggest that  $P_{\text{harv}}$  scales inversely with  $L$  however, from Fig. 13 we see that  $\mathcal{P}$  scales algebraically with  $u$  and hence  $L$  since other parameters are held constant. Our computations suggest that it is possible to increase the harvested power by almost two orders of magnitude either by increasing the cylinder length by  $\approx 30\%$  and retaining a circular cross-section or by replacing with an elliptical cross-section and increasing the cylinder length by  $\approx 20\%$ .

## 5. Conclusions

The objective of this work is to develop a simplified model that includes the principal physical components that contribute to flutter oscillations in slender, flexible cylinders in a bulk flow. By employing the model to understand fundamental aspects related to energy harvesting from mechanical oscillations that arise from fluid–structure instabilities we can attempt to interpret its scope for practical applications.

Flutter oscillations occur when the structure absorbs energy from the fluid. We show that it is the inviscid component of the fluid that is responsible for the instability; these inviscid forces lead to finite amplitude oscillations that are

observed for a certain range of flow speeds and it is this mechanism that is responsible for flutter regardless of geometry and other configurations. Inclusion of the viscous contribution of the fluid extends the range of flow speeds for which flutter is observed, however the fundamental physics corresponding to these flutter oscillations is virtually unchanged. The prediction based on the inviscid analysis that  $c_1$  is the only important energy harvesting parameter remains valid even with the inclusion of drag. The inviscid model is thus shown to be a powerful tool in analysing the dominant physics of complicated systems.

We see that viscous drag has a dual influence on energy harvesting: at a given flow speed its dissipative action reduces the power output; however, the stabilising action of drag leads to sustained limit cycle oscillations at higher values of flow speed. Furthermore, in the high flow speed range, asymmetric modes are triggered in the presence of structural damping. In this study we have only performed a cursory examination of the dynamical characteristics of the system, nonetheless two facts emerge: (a) the asymmetric flutter mode is associated with a growth in the frequency of oscillation for increasing levels of dashpot damping and (b) for  $m_a < 1$ , we can employ this mode to harvest greater levels of power. Estimates of the dimensional power that can be harvested suggest that a circular cylinder of 1 m length immersed in a flowstream of  $\sim 1$  m/s would harvest power of the order of a few milliwatts. However, the harvested power increases by almost two orders of magnitude with a 20% increase in length and a switch to an elliptical cross-section.

The primary appeal of this bi-articulated system under investigation as an energy harvesting device is the demonstrated simplicity of harvesting the energy of self-sustained oscillations from a slender flexible structure in an axial flowstream. An important result from this analysis is that a single harvester at the fixed end (with an optimal value of damping coefficient) can extract the maximum available power from the system. Conversely, an additional dashpot at the articulation  $P$  would mitigate the flutter instability and reduce the total harvested power.

Our analysis shows the theoretical feasibility of energy harvesting from such a system, which motivates an extension of the analysis to a continuously flexible cylinder. A key insight gained from this analysis with a reduced order model of a flexible cylinder in an axial flow is that energy harvesters ought to be distributed non-homogeneously along the length. The optimal distribution of damping for a continuous system that will lead to maximum energy harvesting is a topic for further investigation.

## Acknowledgements

The authors gratefully acknowledge Electricité de France (EDF) for their support through the ‘Chaire Energies Durables’ at the École Polytechnique.

## References

- Alben, S., Shelley, M., 2008. Flapping states of a flag in an inviscid fluid: bistability and the transition to chaos. *Physical Review Letters* 100 (074301).
- Benjamin, T.B., 1961a. Dynamics of a system of articulated pipes conveying fluid. (I). Theory. *Proceedings of the Royal Society A* 261, 457–486.
- Benjamin, T.B., 1961b. Dynamics of a system of articulated pipes conveying fluid. (II). Experiments. *Proceedings of the Royal Society A* 261, 487–499.
- Boyer, F., Porez, M., Leroyer, A., Visonneau, M., 2008. Fast dynamics of an eel-like robot—comparisons with Navier–Stokes simulations. *IEEE Transactions on Robotics* 24, 1274–1288.
- Bryant, M., Garcia, E., 2011. Modeling and testing of a novel aeroelastic flutter energy harvester. *Journal of Vibrations & Acoustics* 133, 12.1–12.11.
- Candelier, F., Boyer, F., Leroyer, A., 2011. Three-dimensional extension of Lighthill’s large-amplitude elongated-body theory of fish locomotion. *Journal of Fluid Mechanics* 674, 196–226.
- Crighton, D.G., Oswell, J.E., 1991. Fluid loading with mean flow. (I). Response of an elastic plate to localized excitation. *Philosophical Transactions of Royal Society London, A* 335, 557–592.
- de Langre, E., Doaré, O., Païdoussis, M.P., Modarres-Sadeghi, Y., 2007. Flutter of long flexible cylinders in axial flow. *Journal of Fluid Mechanics* 571, 371–389.
- Doaré, O., 2010. Dissipation effect on local and global stability of fluid-conveying pipes. *Journal of Sound and Vibration* 329, 72–83.
- Doaré, O., Michelin, S., 2011. Piezoelectric energy harvesting from flutter instability: local/global linear stability and efficiency. *Journal of Fluids and Structures* 27, 1357–1375.
- Dunmon, J.A., Stanton, S.C., Mann, B.P., Dowell, E.H., 2011. Power extraction from aeroelastic limit cycle oscillations. *Journal of Fluids and Structures* 1, 1–17, doi:10.1016/j.jfluidstructs.2011.02.003.
- Eloy, C. Optimal Strouhal number for swimming animals. *Journal of Fluids and Structures*, in press.
- Eloy, C., Souilliez, C., Schouveiler, L., 2007. Flutter of a rectangular plate. *Journal of Fluids and Structures* 23, 904–919.
- Fairley, P., March 2010. Wave Energy Scales Up Off Scotland. *Technology Review*.
- Kambe, T., 1978. The dynamics of carangiform swimming motions. *Journal of Fluid Mechanics* 87 (3), 533–560.
- Landau, L.D., Lifshitz, E.M., 1976. *Mechanics*. Course of Theoretical Physics, third ed., vol. 1. Elsevier Ltd.
- Lemaitre, C., Hémon, P., de Langre, E., 2005. Instability of a long ribbon hanging in axial air flow. *Journal of Fluids and Structures* 20, 913–925.
- Lighthill, M.J., 1960. Note on swimming of slender fish. *Journal of Fluid Mechanics* 9 (Part2), 305–317.
- Lighthill, M.J., 1971. Large-amplitude elongated-body theory of fish locomotion. *Proceedings of the Royal Society* 179, 125–138.
- Lopes, J.L., Païdoussis, M.P., Semler, C., 2002. Linear and nonlinear dynamics of cantilevered cylinders in axial flow. Part 2. The of motion. *Journal of Fluids and Structures* 16, 715–739.
- Lucey, A.D., Cafolla, G.J., Carpenter, P.W., Yang, M., 1997. The nonlinear hydroelastic behaviour of flexible walls. *Journal of Fluids and Structures* 11, 717–744.
- Michelin, S., Llewellyn Smith, S.G., Glover, B., 2008. Vortex shedding model of a flapping flag. *Journal of Fluid Mechanics* 617, 1–10.
- Païdoussis, M.P., 1998. *Fluid–Structure Interactions: Slender Structures and Axial Flow*, vol. 1. Academic Press, London.
- Païdoussis, M.P., 2004. *Fluid–Structure Interactions: Slender Structures and Axial Flow*, vol. 2. Elsevier Academic Press, London.
- Païdoussis, M.P., Grinevich, E., Adamovic, D., Semler, C., 2002. Linear and nonlinear dynamics of cantilevered cylinders in axial flow. Part 1. Physical dynamics. *Journal of Fluids and Structures* 16, 691–713.
- Peake, N., 2001. Nonlinear stability of a fluid-loaded elastic plate with mean flow. *Journal of Fluid Mechanics* 434, 101–118.

- Semler, C., Lopes, J.L., Augu, N., Païdoussis, M., 2002. Linear and nonlinear dynamics of cantilevered cylinders in axial flow, part 3: nonlinear dynamics. *Journal of Fluids and Structures* 16, 739–759.
- Sherman, F.S., 1990. *Viscous Flow*. McGraw-Hill.
- Taylor, G.I., 1952. Analysis of the swimming of long and narrow animals. *Proceedings of the Royal Society A*, 158–183.
- Westwood, A., 2004. Ocean power: wave and tidal energy review. *Refocus* 5 (5), 50–55.